Kardar-Parisi-Zhang Interfaces with Curved Initial Shapes and Variational Formula

Yohsuke T. Fukai[1,2,*] and Kazumasa A. Takeuchi[2,3,†]

[1]Nonequilibrium Physics of Living Matter RIKEN Hakubi Research Team, RIKEN Center for Biosystems Dynamics Research, 2-2-3 Minatojima-minamimachi, Chuo-ku, Kobe, Hyogo 650-0047, Japan

[2]Department of Physics, The University of Tokyo, 7-3-1 Hongo, Bunkyo-ku, Tokyo, 113-0033, Japan

[3]Department of Physics, Tokyo Institute of Technology, 2-12-1 Ookayama, Meguro-ku, Tokyo, 152-8551, Japan

(Received 26 September 2019; revised manuscript received 27 November 2019; accepted 8 January 2020; published 10 February 2020)

We study fluctuations of interfaces in the Kardar-Parisi-Zhang (KPZ) universality class with curved initial conditions. By simulations of a cluster growth model and experiments with liquid-crystal turbulence, we determine the universal scaling functions that describe the height distribution and the spatial correlation of the interfaces growing outward from a ring. The scaling functions, controlled by a single dimensionless time parameter, show crossover from the statistical properties of the flat interfaces to those of the circular interfaces. Moreover, employing the KPZ variational formula to describe the case of the ring initial condition, we find that the formula, which we numerically evaluate, reproduces the numerical and experimental results precisely without adjustable parameters. This demonstrates that precise numerical evaluation of the variational formula is possible at all, and underlines the practical importance of the formula, which is able to predict the one-point distribution of KPZ interfaces for general initial conditions.

DOI: 10.1103/PhysRevLett.124.060601

Efforts on universal behavior associated with scale invariance, which have established important concepts such as the renormalization group and the universality class, now shed light on novel aspects of nonequilibrium fluctuations. In this respect, the Kardar-Parisi-Zhang (KPZ) universality class [1–4] plays a distinguished role, because of the existence of exact solutions and experimental realizations. The KPZ class is also known to arise in a variety of problems: besides growing interfaces and directed polymers as originally proposed [1], it also turned out to be relevant for stochastic particle transport, quantum integrable systems [3,4], and fluctuating hydrodynamics [5], to name but a few.

In the following, let us focus on the one-dimensional case, for which exact studies have been developed, and consider growing interfaces described by the height $h(x,t)$ at position $x \in \mathbb{R}$ and time $t \in \mathbb{R}$. The KPZ class describes scale-invariant fluctuations of growing interfaces in the long-time limit, in general situations without particular symmetries and conservation laws. The hallmarks of the KPZ class are the scaling laws for the fluctuation amplitude $\sim t^{\beta}$ and the correlation length $\sim t^{1/z}$, with universal exponents β and z that take the values $\beta = 1/3$ and $z = 3/2$ for the one-dimensional case [1,2,4]. The height $h(x,t)$ is then generally written, for large t, as

$$h(x,t) \simeq v_\infty t + (\Gamma t)^{1/3}\chi(X,t), \tag{1}$$

where $\chi(X,t)$ is a stochastic variable, $X := x/\xi(t)$ denotes the coordinate rescaled by the correlation length $\xi(t) := (2/A)(\Gamma t)^{2/3}$, and v_∞, Γ, and A are system-dependent parameters. The variable $\chi(X,t)$ is expected to be universal, in the sense that its statistical properties do not depend on microscopic details of the systems. The scaling exponents of the KPZ class have been found in various experimental systems [6], including colonies of living cells [7,8], combusting paper [9], and liquid-crystal turbulence [4,10–12].

Recently, remarkable developments triggered by exact studies [3,4] have unveiled novel aspects of the KPZ class. A particularly important outcome is the geometry dependence, which we describe below. If an interface grows on top of a flat substrate, as usually assumed in simulations, the interface roughens but maintains the globally flat profile. In contrast, if an interface in a plane starts to grow from a point nucleus, say, at $x = 0$, it takes a circular shape with a growing radius. Although this interface becomes flatter and flatter as the radius increases, statistical properties of $\chi(X,t)$ remain distinct from the flat case. Specifically, $\chi(X,t)$ has different asymptotic behavior as follows:

$$\chi(X,t) \xrightarrow{\mathrm{d}} \begin{cases} \mathcal{A}_1(X), & \text{(flat)} \\ \mathcal{A}_2(X) - X^2, & \text{(circular)} \end{cases} \tag{2}$$

where $\xrightarrow{\mathrm{d}}$ denotes convergence in distribution ($\overset{\mathrm{d}}{=}$ and $\overset{\mathrm{d}}{\simeq}$ will be used analogously). $\mathcal{A}_1(X)$ and $\mathcal{A}_2(X)$ are called the Airy$_1$ [13,14] and Airy$_2$ [15] processes, respectively, and are well studied analytically [16]. Due to their translational invariance, as long as one-point properties are concerned, $\mathcal{A}_i(X)$ can be replaced by a single stochastic variable χ_i. Remarkably, the one-point distributions of χ_1 and χ_2 were shown [17–20] to coincide, respectively, with the GOE and

GUE Tracy-Widom distributions [21] known from random matrix theory [22], which describe the distribution of the largest eigenvalue of random matrices in the Gaussian orthogonal and unitary ensembles (GOE and GUE), respectively. This geometry dependence, as well as the emergence of the Tracy-Widom distribution, turned out to be experimentally relevant too, as shown by experiments on liquid-crystal turbulence [4,10,11]. Correlation properties were also shown to be different between the flat and circular cases, even though the scaling exponents β and z take the same values. On the basis of those results, one may state that the flat and circular interfaces constitute different *universality subclasses* within the single KPZ class, characterized by different yet universal distribution and correlation properties.

Those universality subclasses have been, however, mostly studied for a few "canonical" cases including the flat and circular ones. A natural and important question is then what happens for more general initial conditions. Theoretically, the KPZ fixed-point variational formula [16,23–26] can be used to predict the asymptotic properties of $\chi(X, t \to \infty)$ for general initial conditions. On the other hand, experimental and numerical studies have focused on finite-time behavior emerging from intermediate initial conditions. For example, the present authors [12] studied growth from a ring of finite radius R_0, which then produces two curved interfaces, one growing outward and the other one inward. Focusing on the ingrowing interfaces, we found that finite-time properties of $\chi(X, t)$ for different R_0 are controlled solely by the rescaled time $\tau \coloneqq v_\infty t/R_0$, as follows: statistical properties of $\chi(X, t)$ agree with those for the *flat* subclass initially ($\tau \ll 1$), until the interfaces nearly collapse at $\tau \approx 1$ and therefore do not behave as KPZ anymore. Analogous behavior was also observed numerically by Carrasco and Oliveira [27], who used lattice models with system size set to decrease in time (mimicking the shrinking circumference of the ingrowing interfaces). The case of enlarging substrates, which would correspond to the outgrowing case, has also been studied, and crossover from the flat to circular subclasses was suggested in this case [27–29], which is also expected to be described by τ. However, it remains unclear how universal such finite-time behavior is, why τ is the right parameter to describe it, and above all, how such crossover can be described theoretically.

Those problems are addressed and answered in this Letter. We study outgrowing interfaces from ring initial conditions both numerically and experimentally, using an off-lattice version of the Eden model [30] and the liquid-crystal turbulence [4,10–12]. Scaling functions for the flat-to-circular crossover are determined and shown to be the same for both of the studied systems. Moreover, we describe this crossover theoretically, by adapting the variational formula [16,23–26] for curved initial conditions. The formula is numerically evaluated and shown to reproduce our numerical and experimental results quantitatively, without adjustable parameters. This also implies that the flat-to-circular crossover is indeed universal and, furthermore, should generally appear for *any* curved interfaces with locally parabolic initial conditions.

We first study the off-lattice Eden model [30], in which a cluster of round particles (with unit diameter) grows by stochastic addition of new particles. The initial condition is set to be a ring of N particles [Fig. 1(a)]. The evolution rule is as follows (see Ref. [30] for details): At each time step, we randomly choose a particle at the interface, attempt to put a new particle next to it in a random direction, and do so if there is no overlapping particle. Time is then increased by $1/(\text{the number of the interfacial particles})$ whether the new particle was added or not. Particles that cannot contribute further growth are checked and removed from the list of the interfacial particles with every time unit. To characterize the height fluctuations, we measure the local radius increment $R(\theta, t)$, which is the radial distance between the initial ring and the interface at each angular position θ [Fig. 1(a)]. Thanks to the rotational symmetry, we have

$$R(\theta, t) \overset{\mathrm{d}}{=} h(0, t) \simeq v_\infty t + (\Gamma t)^{1/3} \chi(0, t), \tag{3}$$

but statistical precision can be improved by averaging over θ. In our simulations, we varied the initial size N from 100 to 40 000 and obtained 4320 to 14 400 realizations for each case (summarized in Table SI in the Supplemental Material [31]). For comparison, we also simulated flat interfaces, for which the initial condition was a line formed by 75 000 particles and the periodic boundary condition in the spanwise direction was used, and we obtained 14 400 realizations.

To characterize statistical properties of the stochastic variable $\chi(X, t)$, we first estimated the nonuniversal parameters, v_∞, Γ, and A, from the data for the flat interfaces. v_∞ and Γ were obtained by the standard procedure [4]—specifically, by using $\partial_t \langle h \rangle \simeq v_\infty + \text{const} \times t^{-2/3}$ and $\langle h^2 \rangle_c / (t^{2/3} \langle \chi_1^2 \rangle_c) \simeq \Gamma^{2/3}$, where $\langle \cdots^k \rangle_c$ denotes the kth-order cumulant, and here we used the fact that the asymptotic fluctuations of the flat interfaces are given by the GOE Tracy-Widom distribution. We obtained $v_\infty = 0.51370(5)$ and $\Gamma = 0.980(3)$. The parameter A was

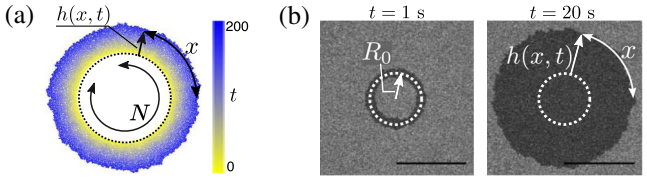

FIG. 1. Typical snapshots from the Eden simulations and the liquid-crystal experiments. (a) An Eden interface growing outward from a ring with $N = 1000$ (dotted line). Time is indicated by the color. (b) A DSM2 cluster (black) growing from a ring with $R_0 = 366$ μm (dotted lines). The elapsed time after shooting the laser is indicated above each image. The scale bar corresponds to 1 mm.

obtained by $A = \sqrt{2\Gamma/v_\infty}$, the relationship valid for isotropic growth [11].

With those parameter values, we define the rescaled height

$$q(\theta,t) \coloneqq \frac{R(\theta,t) - v_\infty t}{(\Gamma t)^{1/3}} \overset{\mathrm{d}}{\simeq} \chi(0,t) \tag{4}$$

and measure its mean and variance as functions of time, for different initial particle numbers N (left panel of Fig. 2). Figure 2 also shows the rescaled mean velocity [4,12]

$$\begin{aligned}\langle p(\theta,t)\rangle &\coloneqq \left\langle \frac{3t^{2/3}}{\Gamma^{1/3}}[\partial_t R(\theta,t) - v_\infty]\right\rangle \\ &\simeq \langle\chi(0,t)\rangle + 3t\partial_t\langle\chi(0,t)\rangle,\end{aligned} \tag{5}$$

which asymptotically goes to $\langle\chi(0,t)\rangle$ if $\langle\chi(0,t)\rangle$ converges sufficiently fast. For the flat case (gray circles), $\langle q\rangle \to \langle\chi_1\rangle$, $\langle p\rangle \to \langle\chi_1\rangle$, and $\langle q^2\rangle_c \to \langle {\chi_1}^2\rangle_c$ as expected. In the case of the ring initial conditions, for large N, the data first behave similarly to the flat case, then deviate and approach the values for the circular subclass, $\langle\chi_2\rangle$ and $\langle\chi_2^2\rangle_c$ [37]. This crossover takes place earlier for smaller N. Indeed, when the data are plotted against the rescaled time $\tau = v_\infty t/R_0$ ($R_0 = N/2\pi$), all data collapse onto a single curve except for the nonuniversal short-time regime (right panel of Fig. 2). This suggests that the distribution of $\chi(0,t)$ for different R_0's, denoted by $\chi(0,t;R_0)$, is described by a single stochastic variable $\chi_c(0,\tau)$, parametrized by τ, as follows:

$$\chi(0,t;R_0) \xrightarrow{\mathrm{d}} \chi_c(0,\tau), \qquad (R_0, t \to \infty), \tag{6}$$

where the double limit is taken with fixed $\tau = v_\infty t/R_0$. Then the flat-to-circular crossover we found indicates $\chi_c(0,\tau) \xrightarrow{\mathrm{d}} \chi_1$ for $\tau \to 0$ and $\chi_c(0,\tau) \xrightarrow{\mathrm{d}} \chi_2$ for $\tau \to \infty$. The skewness $\mathrm{Sk}[R(\theta,t)] \coloneqq \langle R^3\rangle_c/\langle R^2\rangle_c^{3/2} \to \mathrm{Sk}[\chi_c(0,\tau)]$ and the kurtosis $\mathrm{Ku}[R(\theta,t)] \coloneqq \langle R^4\rangle_c/\langle R^2\rangle_c^2 \to \mathrm{Ku}[\chi_c(0,\tau)]$ show consistent behavior (see Fig. S1 in the Supplemental Material [31]).

We also study this crossover in the spatial correlation. In the case of the point initial condition, suppose $\theta = 0$ corresponds to $x = 0$. Then, using $R(\theta,t) = \sqrt{h(x,t)^2 + x^2} \simeq h + x^2/2h$ and Eq. (2), we can show $q(\theta,t) \xrightarrow{\mathrm{d}} \mathcal{A}_2(X)$. Therefore, the rescaled spatial covariance, $C_s(\Delta X,t) \coloneqq \langle q(\theta+\Delta\theta,t)q(\theta,t)\rangle - \langle q(\theta,t)\rangle^2$ with $\Delta X \coloneqq \langle R(\theta,t)\rangle\Delta\theta/\xi(t)$, can be directly compared with the covariance of the Airy_1 and Airy_2 processes. Our numerical results for the ring initial conditions (filled symbols in Fig. S2 of the Supplemental Material [31]) indeed show crossover from the Airy_1 covariance ($\tau \ll 1$) to the Airy_2 covariance ($\tau \gg 1$), consistent with the results on the one-point distribution.

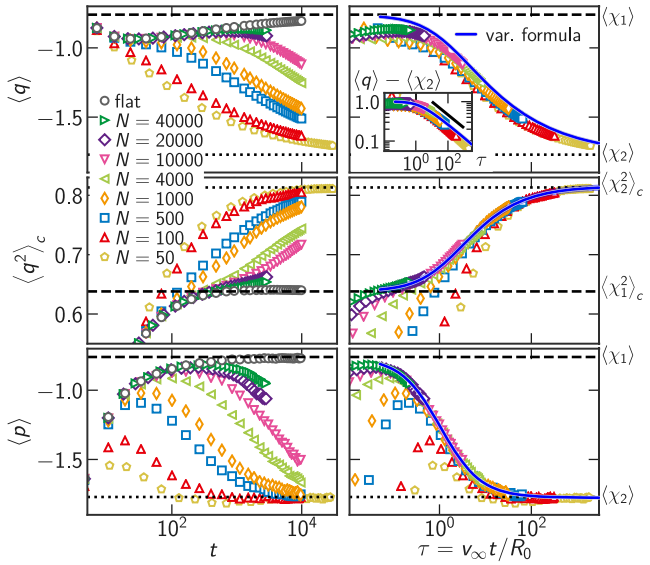

FIG. 2. The mean and variance of the rescaled height, $\langle q(\theta,t)\rangle$ and $\langle q(\theta,t)^2\rangle_c$, and the rescaled mean velocity, $\langle p(\theta,t)\rangle$, for the Eden model in the outgrowing case. The data are shown against the raw time t (left) and the rescaled time $\tau = v_\infty t/R_0$ (right). The theoretical curves evaluated numerically from the variational formula for the outgrowing interfaces (= var. formula, blue solid line) are shown in the right panels. The values of χ_1 and χ_2 are shown by the dashed and dotted lines, respectively. The inset of the top-right figure shows the difference between the data and the excepted long-time limit value, $\langle\chi_2\rangle$. The black solid line indicates slope $-1/3$.

To test the universality of our finding, and in particular, the function forms of $\langle\chi_c(0,\tau)\rangle$ and $\langle\chi_c(0,\tau)^2\rangle_c$, we conducted experiments on liquid-crystal turbulence [4,10–12]. As in the previous studies, we applied an ac voltage (here, 22 V at 300 Hz) to a nematic liquid crystal filling a thin gap between transparent electrodes, and we observed the growth of a turbulent state called dynamic scattering mode 2 (DSM2), expanding in a metastable turbulent state, DSM1 (see the Supplemental Material [31] for detailed methods). DSM2 was generated by emitting a few ultraviolet laser pulses [4]. Using the holographic technique we previously adopted for the DSM2 growth experiments [12], we formed the laser intensity profile in the shape of a ring of a given radius R_0, which sets the initial condition of the DSM2 interface [Fig. 1(b)]. We also generated circular interfaces with a point initial condition, and flat interfaces with a linear initial condition. We obtained 941 to 1936 realizations for each case (see Table SII in the Supplemental Material [31]), recorded by a charge-coupled device camera. The radius $R(\theta,t)$ of the DSM2 interfaces [or the height $h(x,t)$ for the flat case] was determined from each image, with the time t defined as the elapsed time after shooting the laser pulses. Then the nonuniversal parameters v_∞, Γ, and A were evaluated in the same way as for the Eden model, here for the flat and point initial conditions (Table SII [31]). Although the values of

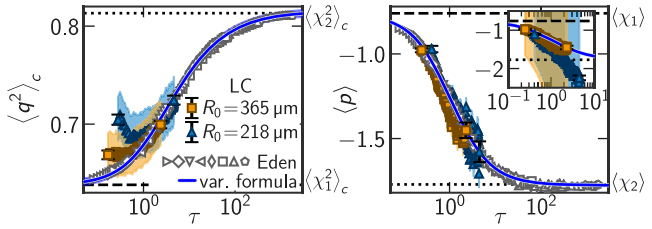

FIG. 3. Comparison of the results from the experiments (color-filled symbols), the Eden simulations (gray open symbols), and the variational formula (= var. formula, blue solid line), for the outgrowing interfaces. The variance of the rescaled height, $\langle q(\theta,t)^2\rangle_c$, and the rescaled mean velocity $\langle p(\theta,t)\rangle$ are shown in the left and right panels, respectively, against $\tau = v_\infty t/R_0$. For the numerical results, data with $t > 10^3$ are shown by the same symbols as those in Fig. 2. For the experimental results, statistical errors are indicated by the error bars on the first and last data points, and uncertainty associated with the parameter estimation is shown by the shaded areas. The values for χ_1 (flat) and χ_2 (circular) are shown by the dashed and dotted lines, respectively. The inset of the right panel shows the experimental results obtained with v_∞ from the flat case, while it was adjusted in the main panel to fit the Eden data at the largest t (see text).

v_∞, Γ, and A are expected to be independent of the initial condition, in practice one needs to evaluate for each set of experiments, because of unavoidable slight changes in experimental conditions [11]. For the ring initial conditions, however, the parameter values could not be obtained in the same way because of the time dependence (i.e., crossover) of $\chi(X,t)$. We therefore used the values obtained from the flat case for the outgrowing cases, unless otherwise stipulated. Possible shifts in the parameter values were taken into account in the uncertainty estimates for the outgrowing cases, evaluated from the differences in the parameter values between the flat and circular cases.

Now, we compare the experimental results with those for the Eden model. The left panel of Fig. 3 shows the variance of the rescaled height, $\langle q(\theta,t)^2\rangle_c$, against $\tau = v_\infty t/R_0$, which overlaps on the Eden data within statistical errors and parameter uncertainty (error bars and shades, respectively) apart from the nonuniversal short-time behavior. For the rescaled mean velocity $\langle p(\theta,t)\rangle$ (right panel), the uncertainty of v_∞ was too large to make a meaningful comparison (inset). However, if we instead choose the value of v_∞ in such a way that $\langle p(\theta,t)\rangle$ at the largest t falls onto the curve for the Eden model (obtained values of v_∞ are given in Table SII [31]), $\langle p(\theta,t)\rangle$ overlaps for *all* t (main panel). Those results of $\langle q(\theta,t)^2\rangle_c$ and $\langle p(\theta,t)\rangle$ suggest universality of the one-point distribution of $\chi_c(0,\tau)$. Moreover, the spatial covariance $C_s(\Delta X,t)$ is also found to overlap with the results of the Eden model if the value of τ is close enough (Fig. S2 [31]). This suggests that not only the one-point distribution of $\chi_c(0,\tau)$, but also the spatial covariance of $\chi_c(X,\tau)$, is universal.

So far, we have characterized the flat-to-circular crossover and found it to be controlled by a single parameter $\tau = v_\infty t/R_0$. But why so, and how can this crossover be theoretically described? To answer these questions, we employ the variational formula [16,23–26] and apply it to a general, curved initial condition.

The variational formula describes the height $h(x,t)$ for a general initial condition $h(x,0) =: h_0(x)$ as follows:

$$h(x,t) \overset{\mathrm{d}}{\cong} \sup_{y\in\mathbb{R}} [h_{\mathrm{circ}}(x,t;y) + h_0(y)], \tag{7}$$

where $h_{\mathrm{circ}}(x,t;y)$ denotes the height for the point initial condition nucleating at position y, growing with the same realization of noise for different y [23]. Intuitively, this means that the initial condition $h(x,0)$ can be regarded as a collection of point sources, and $h(x,t)$ is then given by the envelope of the circular interfaces from those point sources, a bit analogously to Huygens' principle [38]. The formula (7) involves a mathematical object called the Airy sheet [23,25], but if the interest is only in the one-point distribution, it can be simply expressed by the Airy_2 process, as follows [16,24]:

$$\chi(X,t) \overset{\mathrm{d}}{\cong} \sup_{Y\in\mathbb{R}} \left[\mathcal{A}_2(X-Y) - (X-Y)^2 + \frac{h_0(\xi(t)Y)}{(\Gamma t)^{1/3}}\right]. \tag{8}$$

We use Eq. (8) and consider a class of curved initial conditions in the following form:

$$h_0(x) = R_0 g\left(\frac{x}{R_0}\right), \tag{9}$$

where $g(w)$ is a locally parabolic function, i.e., $g(w) = -c_2 w^2 + \mathcal{O}(w^2)$ for small $|w|$. Substituting Eq. (9) into Eq. (8), taking the limit $R_0, t \to \infty$ with fixed $\tau = v_\infty t/R_0$, and setting $x = 0$ yields

$$\chi(0,t) \xrightarrow{\mathrm{d}} \sup_{Y\in\mathbb{R}} [\mathcal{A}_2(Y) - (1+c\tau)Y^2] =: \tilde{\chi}(c\tau), \tag{10}$$

with $c := (4c_2\Gamma)/(A^2 v_\infty)$. This shows that the asymptotic height distribution is parametrized only by $c\tau$, and only the local functional form of $g(w)$ at small $|w|$ is relevant. The characteristic time is $\tau = 1/c$ in the rescaled unit, and therefore $t = A^2 R_0/4c_2\Gamma$ in the raw time scale, and this is the time at which the initial height difference $|h_0(0) - h_0(\xi(t))|$ becomes comparable to the fluctuation amplitude, $(\Gamma t)^{1/3}$. For isotropic growth, the relationship $A = \sqrt{2\Gamma/v_\infty}$ [11] further yields $c = 2c_2$.

For the ring initial conditions, $g(w)$ is given by $g(w) = \sigma(\sqrt{1-w^2}\mathbb{1}_{|w|<1} - 1)$ with $\sigma = +1$ (-1) for the outgrowing (ingrowing) case. Then we obtain $\chi(0,t) \overset{\mathrm{d}}{\cong} \tilde{\chi}(\sigma\tau)$, which we have expressed by $\chi_c(0,\tau)$ for the outgrowing case $\sigma = +1$ [Eq. (6)]. Note that, mathematically, it is known that $\tilde{\chi}(0) = \sup_{Y\in\mathbb{R}}(\mathcal{A}_2(Y) - Y^2) \overset{\mathrm{d}}{=} \chi_1$; i.e., the GOE Tracy-Widom distribution [39,40]. In the other limit

$\tau \to \infty$, clearly, $\tilde{\chi}(\tau) \to \mathcal{A}_2(0) \overset{\mathrm{d}}{=} \chi_2$; i.e., the GUE Tracy-Widom distribution. Therefore, $\chi_{\mathrm{c}}(0,\tau) = \tilde{\chi}(\tau)$ indeed has the expected limits on both sides of the flat-to-circular crossover.

To compare the variational formula with the experimental and numerical data for finite τ, we employ a Monte Carlo method to evaluate Eq. (10). The Airy_2 process $\mathcal{A}_2(Y)$ is in fact known to be equivalent to the largest eigenvalue of large GUE random matrices undergoing Dyson's Brownian motion [16,39]. We therefore implement Dyson's Brownian motion numerically, in the form of the Ornstein-Uhlenbeck process of Hermitian random matrices and obtain approximated realizations of $\mathcal{A}_2(Y)$ (see the Supplemental Material [31] for details). Then, we evaluate the supremum of Eq. (10), interpolating the values of $\mathcal{A}_2(Y)$ between the discrete steps by using the Brownian bridge [31]. The results for the outgrowing case ($\sigma = +1$) are shown in Figs. 2 and 3, where the data of the mean $\langle q \rangle$, the variance $\langle q^2 \rangle_{\mathrm{c}}$, and the rescaled mean velocity $\langle p \rangle$ are compared with the corresponding expressions of $\tilde{\chi}(\tau)$—specifically, $\langle \tilde{\chi}(\tau) \rangle$, $\langle \tilde{\chi}(\tau)^2 \rangle_{\mathrm{c}}$ [Eq. (4)], and $\langle \tilde{\chi}(\tau) \rangle + 3\tau \partial_\tau \langle \tilde{\chi}(\tau) \rangle$ [Eq. (5)], respectively. The results of the variational formula precisely agree, without any adjustable parameter, with the numerical and experimental data. We also inspected the ingrowing case $\sigma = -1$ and confirmed the validity of the variational formula (see Fig. S3 of the Supplemental Material [31]). The agreement was also underpinned for the skewness and kurtosis (Fig. S4 of the Supplemental Material [31]).

In summary, we found KPZ crossover functions that govern height fluctuations of interfaces growing outward from ring initial conditions, parametrized only by the rescaled time $\tau = v_\infty t/R_0$, and evidenced their universality both experimentally and numerically. We then presented a theoretical description of this crossover, on the basis of the KPZ variational formula for general curved initial conditions. We numerically evaluated the formula and found remarkable agreement with the experimental and numerical data. Our results constitute the first example where the KPZ variational formula was successfully used to describe experimental observations, showing the ability of this formula to explain, or even predict, real data from general initial conditions. We hope our work will trigger further studies to elucidate geometry-dependent universality of the KPZ class and beyond.

We thank P. Le Doussal for useful discussions on the variational formula, and F. Bornemann for the theoretical curves of the Airy_1 and Airy_2 covariance [41]. We thank the Supercomputer Center of the Institute for Solid State Physics (the University of Tokyo) and the Meiji Institute for Advanced Study of Mathematical Sciences (Meiji University) for computational facilities. We acknowledge financial support by KAKENHI from the Japan Society for the Promotion of Science (Grants No. JP25103004, No. JP16H04033, No. JP19H05800, No. JP19H05144, No. JP17J05559), by the Yamada Science Foundation, and by the National Science Foundation (Grant No. NSF PHY11-25915).

*ysk@yfukai.net
†kat@kaztake.org

[1] M. Kardar, G. Parisi, and Y.-C. Zhang, Phys. Rev. Lett. **56**, 889 (1986).
[2] A.-L. Barabási and H. Eugene Stanley, *Fractal Concepts in Surface Growth* (Cambridge University Press, New York, NY, USA, 1995).
[3] For recent reviews, see, e g., T. Kriecherbauer and J. Krug, J. Phys. A **43**, 403001 (2010); I. Corwin, Random Matrices Theory Appl. **01**, 1130001 (2012); J. Quastel and H. Spohn, J. Stat. Phys. **160**, 965 (2015); T. Halpin-Healy and K. A. Takeuchi, J. Stat. Phys. **160**, 794 (2015); T. Sasamoto, Prog. Theor. Exp. Phys. **2016**, 022A01 (2016).
[4] For lecture notes, see K. A. Takeuchi, Physica (Amsterdam) **504A**, 77 (2018).
[5] H. Spohn, in *Thermal Transport in Low Dimensions*, Lecture Notes in Physics Vol. 921 (Springer International Publishing, Cham, 2016), pp. 107–158, https://doi.org/10.1007/978-3-319-29261-8_3.
[6] K. A. Takeuchi, J. Stat. Mech. (2014) P01006.
[7] J.-i. Wakita, H. Itoh, T. Matsuyama, and M. Matsushita, J. Phys. Soc. Jpn. **66**, 67 (1997).
[8] M. A. C. Huergo, M. A. Pasquale, A. E. Bolzán, A. J. Arvia, and P. H. González, Phys. Rev. E **82**, 031903 (2010); M. A. C. Huergo, M. A. Pasquale, P. H. González, A. E. Bolzán, and A. J. Arvia, Phys. Rev. E **84**, 021917 (2011); **85**, 011918 (2012).
[9] J. Maunuksela, M. Myllys, O.-P. Kähkönen, J. Timonen, N. Provatas, M. J. Alava, and T. Ala-Nissila, Phys. Rev. Lett. **79**, 1515 (1997).
[10] K. A. Takeuchi and M. Sano, Phys. Rev. Lett. **104**, 230601 (2010); K. A. Takeuchi, M. Sano, T. Sasamoto, and H. Spohn, Sci. Rep. **1**, 34 (2011).
[11] K. A. Takeuchi and M. Sano, J. Stat. Phys. **147**, 853 (2012).
[12] Y. T. Fukai and K. A. Takeuchi, Phys. Rev. Lett. **119**, 030602 (2017).
[13] T. Sasamoto, J. Phys. A **38**, L549 (2005).
[14] A. Borodin, P. L. Ferrari, M. Prähofer, and T. Sasamoto, J. Stat. Phys. **129**, 1055 (2007).
[15] M. Prähofer and H. Spohn, J. Stat. Phys. **108**, 1071 (2002).
[16] J. Quastel and D. Remenik, in *Topics in Percolative and Disordered Systems*, Springer Proceedings in Mathematics & Statistics Vol. 69 (Springer, New York, 2014), pp. 121–171, https://doi.org/10.1007/978-1-4939-0339-9_5.
[17] J. Baik, P. Deift, and K. Johansson, J. Am. Math. Soc. **12**, 1119 (1999).
[18] K. Johansson, Commun. Math. Phys. **209**, 437 (2000).
[19] J. Baik and E. M. Rains, in *Random Matrix Models and Their Applications*, MSRI Publications, Vol. 40, edited by P. Bleher and A. Its (Cambridge University Press, Cambridge, England, 2001), pp. 1–19.

[20] M. Prähofer and H. Spohn, Physica (Amsterdam) **279A**, 342 (2000); Phys. Rev. Lett. **84**, 4882 (2000).
[21] C. A. Tracy and H. Widom, Commun. Math. Phys. **159**, 151 (1994); **177**, 727 (1996).
[22] G. W. Anderson, A. Guionnet, and O. Zeitouni, in *An Introduction to Random Matrices*, Cambridge Studies in Advanced Mathematics Vol. 118 (Cambridge University Press, Cambridge, England, 2010), https://doi.org/10.1017/CBO9780511801334.
[23] I. Corwin, J. Quastel, and D. Remenik, J. Stat. Phys. **160**, 815 (2015).
[24] I. Corwin, Z. Liu, and D. Wang, Ann. Appl. Probab. **26**, 2030 (2016).
[25] D. Dauvergne, J. Ortmann, and B. Virág, arXiv:1812.00309.
[26] J. Quastel and D. Remenik, Trans. Am. Math. Soc. **371**, 6047 (2019).
[27] I. S. S. Carrasco and T. J. Oliveira, Phys. Rev. E **98**, 010102 (R) (2018).
[28] I. S. S. Carrasco, K. A. Takeuchi, S. C. Ferreira, and T. J. Oliveira, New J. Phys. **16**, 123057 (2014).
[29] I. S. S. Carrasco and T. J. Oliveira, Phys. Rev. E **99**, 032140 (2019).
[30] K. A. Takeuchi, J. Stat. Mech. (2012) P05007.
[31] See Supplemental Material at http://link.aps.org/supplemental/10.1103/PhysRevLett.124.060601 for the detailed experimental methods, numerical evaluation of the variational formula, Tables SI and SII, and Figs. S1, S2, S3, S4, and S5, which includes Refs. [32–36].
[32] P. G. de Gennes and J. Prost, *The Physics of Liquid Crystals* (Oxford University Press, Oxford, 1995).
[33] D. T. Gillespie, Phys. Rev. E **54**, 2084 (1996).
[34] J. Hägg, Ann. Probab. **36**, 1059 (2008).
[35] L. Beghin and E. Orsingher, Lith. Math. J. **39**, 157 (1999).
[36] I. M. Johnstone and Z. Ma, Ann. Appl. Probab. **22**, 1962 (2012).
[37] Though the value of $\langle q \rangle$ does not fully converge to $\langle \chi_2 \rangle$ even at the largest τ we reached, the difference seems to converge to zero with a power law with an exponent close to $-1/3$ (inset of Fig. 2). This suggests convergence of $\langle q \rangle$ to $\langle \chi_2 \rangle$ in the limit of $t \to \infty$.
[38] Though nonlinear equations generally do not admit the principle of superposition, the KPZ equation can be mapped to a linear equation by the Cole-Hopf transformation, and this leads to the variational formula (7) [16].
[39] K. Johansson, Commun. Math. Phys. **242**, 277 (2003).
[40] I. Corwin, J. Quastel, and D. Remenik, Commun. Math. Phys. **317**, 347 (2013).
[41] F. Bornemann, Math. Comput. **79**, 871 (2010).

Supplemental Material for Kardar-Parisi-Zhang Interfaces with Curved Initial Shapes and Variational Formula

Yohsuke T. Fukai[1, 2, *] and Kazumasa A. Takeuchi[2, †]

[1] *RIKEN Center for Biosystems Dynamics Research*
[2] *Department of Physics, the University of Tokyo*

JANUARY 9, 2020

SUPPLEMENTAL TEXT 1: EXPERIMENTAL METHODS

Similarly to the past studies [1–5], we prepared an electroconvection cell by assembling two glass plates with transparent electrodes, sandwiching 12 µm-thickness spacers. A liquid-crystal sample, *N*-(4-Methoxybenzylidene)-4-butylaniline doped with 0.01wt.% of tetra-*n*-butylammonium bromide, was filled in a 1.5 cm × 1.5 cm region enclosed by the spacers. The homeotropic alignment was achieved by spin-coating *N*,*N*-dimethyl-*N*-octadecyl-3-aminopropyltrimethoxysilyl chloride on the electrodes. The cell was contained in a temperature controller, whose temperature was maintained at 25 °C, with the temporal fluctuation in the order of ±0.01 °C. Under this temperature, the electroconvection was observed by applying an AC voltage to the cell. The cutoff frequency, which separates the conductive and dielectric regimes of the electroconvection [6], was roughly 1.7×10^3 Hz. At the frequency we used in the main experiments, 300 Hz, compact DSM2 clusters grew at the amplitude $\gtrsim 17.5$ V. The voltage amplitude for the main experiments, 22 V, was chosen to be sufficiently higher than that threshold.

To generate a growing DSM2 interface, we first applied an AC voltage of amplitude 22 V and frequency 300 Hz to the cell and the system was set entirely in the metastable DSM1 state. After 5 s, we emitted three ultraviolet laser pulses to the cell (New Wave Research MiniLaseII, wavelength 355 nm, pulse width 4-6 ns, repetition frequency 20 Hz, energy $\lessapprox 0.4$ mJ after attenuation) to nucleate DSM2 [4]. The laser pulse was reflected by a spatial light modulator (Hamamatsu Photonics, LCOS-SLM X10468-05) and a hologram of the given shape was made, by using the experimental setup reported in Ref. [5]. For the linear initial condition, the line length was approximately 8 mm. Then the growing DSM2 interface was recorded by a charge-coupled device camera for a given time (for the flat interfaces, the region of width ≈ 4 mm near the center of the line was observed). Then we turned off the applied voltage, waited for 30 s, and started the next run.

To obtain the radius $R(\theta, t)$ of the DSM2 interfaces (or the height $h(x, t)$ for the flat case), we binarized each image by thresholding. For the ring initial conditions, first we determined the center of the ring by using the ensemble average of the image intensity fields taken at $t = 1$ s, and used it to define the radius $R(\theta, t)$.

SUPPLEMENTAL TEXT 2: EVALUATION OF THE VARIATIONAL FORMULA

Detailed description of the numerical method

We evaluated the variational formula (10) by using Dyson's Brownian motion to approximate the Airy_2 process, as follows:

1. We first prepared an initial Hermitian random matrix drawn from the Gaussian unitary ensemble (GUE), or equivalently, the stationary distribution of Eq. (S2) (below):

$$H_{jk}(0) = \begin{cases} \sqrt{\frac{1}{2}}\mathcal{N}_{jk}^{(1)} & (j = k) \\ \frac{1}{2}\left[\mathcal{N}_{jk}^{(1)} + \mathrm{i}\mathcal{N}_{jk}^{(2)}\right] & (j > k) \end{cases}, \tag{S1}$$

   where $\mathcal{N}_{jk}^{(m)}$ are i.i.d. random variables drawn from the normal distribution with the mean 0 and the variance 1.

2. We simulated the following Ornstein-Uhlenbeck process:

$$\frac{\mathrm{d}H_{jk}(u)}{\mathrm{d}u} = \begin{cases} -H_{jk} + \eta_{jk}^{(1)}(u) & (j = k) \\ -H_{jk} + \sqrt{\frac{1}{2}}\left[\eta_{jk}^{(1)}(u) + \mathrm{i}\eta_{jk}^{(2)}(u)\right] & (j > k) \end{cases} \tag{S2}$$

with Gaussian noise $\eta_{jk}^{(m)}(u)$ satisfying $\left\langle \eta_{jk}^{(m)}(u) \right\rangle = 0$ and $\left\langle \eta_{j'k'}^{(m')}(u')\eta_{jk}^{(m)}(u) \right\rangle = \delta_{j'j}\delta_{k'k}\delta_{m'm}\delta(u'-u)$. We employed Gillespie's exact algorithm for the Ornstein-Uhlenbeck process [7] for each element, with time step Δu.

3. We computed the largest eigenvalue $\lambda_j^{(N)} := \lambda^{(N)}(j\Delta u)$ for each time step $j\Delta u$ ($j = 0, \ldots, j_{\max}$). Then, since

$$\sqrt{2}N^{1/6}\left[\lambda^{(N)}(N^{-1/3}Y) - \sqrt{2N}\right] \xrightarrow{\mathrm{d}} \mathcal{A}_2(Y) \qquad (N \to \infty), \tag{S3}$$

we rescaled it as follows:

$$\tilde{\lambda}_j^{(N)} := \sqrt{2}N^{1/6}\left(\lambda_j^{(N)} - \sqrt{2N}\right). \qquad \Delta\tilde{u} := N^{1/3}\Delta u. \tag{S4}$$

4. Using the fact that the Airy$_2$ process is locally equivalent to the Brownian motion with unit diffusion constant (the standard Brownian motion) [8, 9], we approximated the variational formula (10) by

$$\tilde{\chi}(c\tau) = \sup_{Y\in\mathbb{R}}\left[\mathcal{A}_2(Y) - (1+c\tau)Y^2\right] \approx \max_{k=-L,\ldots,L-1} r_k^{(j)} =: \tilde{\chi}_N(c\tau), \tag{S5}$$

where L was taken sufficiently large (see below), $j = L, \ldots, j_{\max} - L$, and $r_k^{(j)}$ is the maximum of the Brownian bridge (with unit diffusion constant) connecting $z_k^{(j)} := \tilde{\lambda}_{j+k}^{(N)} - (1+c\tau)(k\Delta\tilde{u})^2$ and $z_{k+1}^{(j)}$. Specifically, $r_k^{(j)}$ is a random variable whose cumulative distribution function is given by [10]

$$\mathbb{P}\left[r_k^{(j)} < z\right] = \begin{cases} 1 - \exp\left[-\frac{(z-z_k^{(j)})(z-z_{k+1}^{(j)})}{\Delta\tilde{u}}\right] & (z \geq \max\left\{z_k^{(j)}, z_{k+1}^{(j)}\right\}) \\ 0 & (\text{otherwise}). \end{cases} \tag{S6}$$

The range of L was chosen so that it satisfies $\left(\max\tilde{\lambda}_j^{(N)} - \min\tilde{\lambda}_j^{(N)}\right) < (1+c\tau)[(L/1.1)\Delta\tilde{u}]^2$. Then the cumulants $\left\langle \tilde{\chi}_N(c\tau)^k \right\rangle_{\mathrm{c}}$ were evaluated by taking the average of the right-hand side of Eq. (S5) over varying j and independent realizations of the Ornstein-Uhlenbeck process. In our simulations for the main results presented in Figs. 3, S3, and S4, we used 5360 realizations of the Ornstein-Uhlenbeck process with $N = 512$, $\Delta\tilde{u} = 10^{-3}$ (see below), and $j_{\max} = 500000$.

Step size

To find an appropriate step size Δu, we estimated the range of Y that is relevant to the value of the supremum in Eq. (S5). Since the Airy$_2$ process is locally equivalent to the standard Brownian motion, a value of Y such that $(1+c\tau)Y^2$ becomes as large as $\mathcal{A}_2(Y)$, denoted by Y_0, is given approximately by $(1+c\tau)Y_0^2 = \sqrt{2Y_0}$. With this Y_0, $\Delta\tilde{u}$ should be chosen so that $\Delta\tilde{u} \ll Y_0$. For large τ, $Y_0 \approx \tau^{-2/3}$. In the present work, we chose $\Delta\tilde{u} = 10^{-3}$ ($\Delta u = 10^{-3}N^{-1/3}$) so that $\Delta\tilde{u} \ll Y_0$ is satisfied for all $\tau \leq 3 \times 10^3$.

Matrix size N

To quantify the effect of finite matrix size N, we first evaluated the cumulants of the rescaled largest eigenvalue, $\left\langle (\tilde{\lambda}_j^{(N)})^k \right\rangle_{\mathrm{c}}$, with varying N, and compared with the known values for the GUE Tracy-Widom distribution, $\left\langle {\chi_2}^k \right\rangle_{\mathrm{c}}$. The results in Fig. S5(a) show that $\left\langle (\tilde{\lambda}_j^{(N)})^k \right\rangle_{\mathrm{c}}$ indeed approach $\left\langle {\chi_2}^k \right\rangle_{\mathrm{c}}$, with the difference decreasing as $\sim N^{-2/3}$, being consistent with theoretical expectation [11]. Since $\tilde{\chi}_N(\infty) = \tilde{\lambda}_j^{(N)}$, the finite-$N$ corrections shown in Fig. S5(a) are equivalent to those of $\tilde{\chi}(\tau)$ in the limit $\tau \to \infty$. Similarly, we evaluated the variational formula (S5) with $c\tau = 0$, for which it is known that $\tilde{\chi}(0) = \sup_{Y\in\mathbb{R}}(\mathcal{A}_2(Y) - Y^2) \stackrel{\mathrm{d}}{=} \chi_1$, i.e., GOE Tracy-Widom distribution [12, 13]. As displayed in Fig. S5(b), the data obtained from the variational formula indeed show the cumulant values approaching those of χ_1, again with the finite-size corrections proportional to $N^{-2/3}$. From those results, we decided to use

$N = 512$ (largest size) for the main part of the work; at $N = 512$, the amplitude of the finite-N corrections shown in Fig. S5 is small enough to compare with our numerical and experimental data. The uncertainty of the estimated cumulants displayed in Figs. 3, S3, and S4 is the summation of the statistical uncertainty and the expected amplitude of finite-N correction, the latter being evaluated by the larger value of $\left|\left\langle \tilde{\chi}_N\left(\infty\right)^k\right\rangle_{\mathrm{c}} - \left\langle \chi_2^k\right\rangle\right|$ and $\left|\left\langle \tilde{\chi}_N\left(0\right)^k\right\rangle_{\mathrm{c}} - \left\langle \chi_1^k\right\rangle\right|$ [Fig. S5(a) and (b), respectively].

SUPPLEMENTAL TABLES

TABLE SI. Parameters for the Eden simulations.

type	outgrowing					
N	50	100	500	1000	4000	10000
# of samples	14400	14400	14400	14400	11520	4320
type	outgrowing		ingrowing			
N	20000	40000	10000	20000	40000	100000
# of samples	4320	4320	4320	4320	4320	1440
type	flat					
length	75000					
# of samples	14400					

TABLE SII. Experimental conditions and non-universal parameters.

initial condition	# of samples	v_∞(μm/s)	Γ(μm^3/s)
line	1417	30.84(2)	$1.25(2) \times 10^3$
point	941	29.68(3)	$1.31(4) \times 10^3$
$R_0 = 366\,\mu$m	1936	30.84(2)*	–
$R_0 = 219\,\mu$m	1521	30.60(2)*	–

* Values obtained by fitting the last data point of $\langle p \rangle$ to the results of the Eden model (see main text).

SUPPLEMENTAL FIGURES

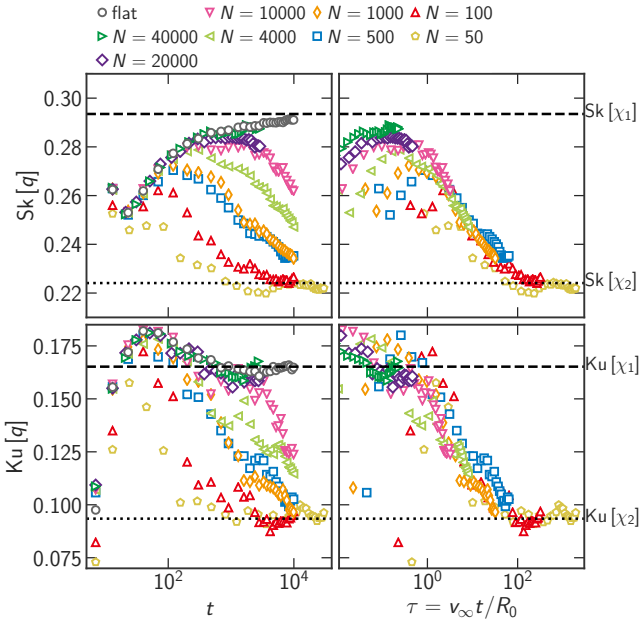

FIG. S1. The skewness and kurtosis of the rescaled height $q(\theta, t)$ for the Eden model. The data are plotted against the raw time t (left column) and the rescaled time $\tau = v_\infty t/R_0$ (right column). The values for χ_1 and χ_2 are shown by the dashed and dotted lines, respectively.

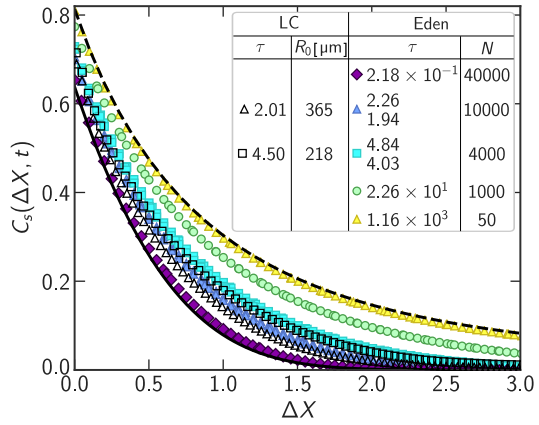

FIG. S2. Spatial covariance $C_s(\Delta X, t)$, plotted against the normalized length ΔX, for the outgrowing interfaces. The solid and dashed lines indicate the Airy$_1$ (flat) and Airy$_2$ (circular) covariance, respectively, $\langle \mathcal{A}_i(X + \Delta X)\mathcal{A}_i(X)\rangle - \langle \mathcal{A}_i(X)\rangle^2$.

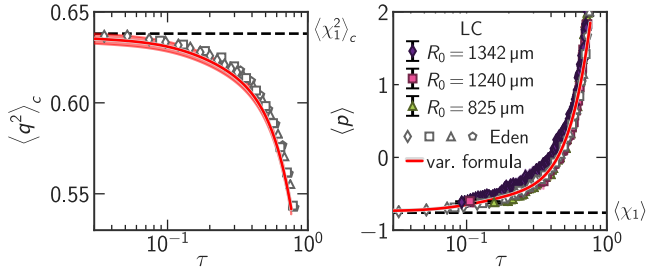

FIG. S3. The ingrowing counterpart of Fig. 3. Results from the liquid-crystal experiments (color filled symbols; data adopted from Ref. [5]) and those from Eden simulations [gray open symbols; $N = 100000(\diamond), 40000(\square), 20000(\triangle), 10000(\pentagon)$] are compared with the curves obtained from the variational formula (=var., red solid line). The shaded area behind the variational formula curves indicates uncertainty of the Monte-Carlo evaluation. See Table SI for the number of realizations for the simulations. The experimental data for the variance (left) is omitted because of large finite-time effect [5]. The values for χ_1 (flat) are shown by the dashed lines.

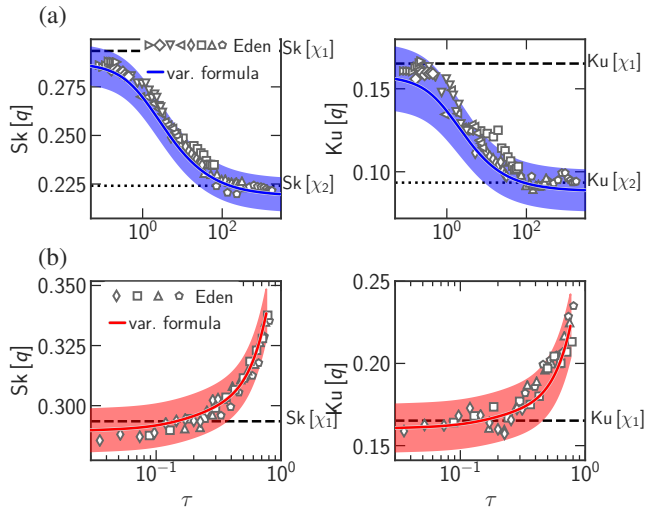

FIG. S4. The skewness and kurtosis of the rescaled height $q(\theta, t)$, plotted against the rescaled time $\tau = v_\infty t/R_0$ for the (a) outgrowing and (b) ingrowing interfaces. The numerical results with $t > 10^3$ are shown by gray open symbols, and the curves obtained by numerical evaluation of the variational (=var.) formula are drawn with the red solid line. The symbols for the numerical results are for the samples with $N = 40000(\triangleright), 20000(\diamond), 10000(\triangledown), 4000(\triangleleft), 1000(\diamond), 500(\square), 100(\triangle), 50(\pentagon)$ for the outgrowing interfaces, and for $N = 100000(\triangleleft), 40000(\diamond), 20000(\square), 10000(\triangle)$ for the ingrowing interfaces, respectively. The shaded area for the variational formula indicates uncertainty of the Monte-Carlo evaluation. The values for χ_1 (flat) and χ_2 (circular) are shown by the dashed and dotted lines, respectively.

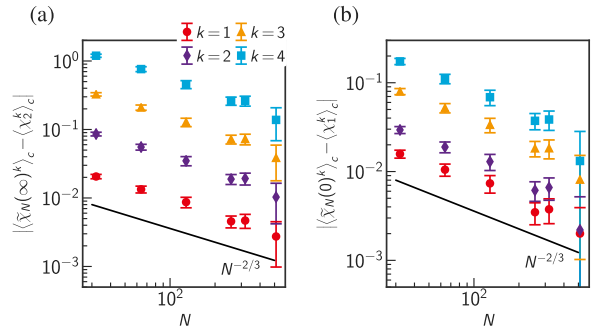

FIG. S5. Finite-N corrections in the cumulants of $\tilde{\chi}_N(\infty) = \tilde{\lambda}_j^{(N)}$ (a) and $\tilde{\chi}_N(0)$ (b). They are compared with the cumulants of χ_2 and χ_1, respectively. The errorbars indicate statistical uncertainty. The black solid lines are guides for the eyes showing the exponent $-2/3$.

* ysk@yfukai.net
† kat@kaztake.org

[1] K. A. Takeuchi and M. Sano, Phys. Rev. Lett. **104**, 230601 (2010).
[2] K. A. Takeuchi, M. Sano, T. Sasamoto, and H. Spohn, Sci. Rep. **1**, 34 (2011).
[3] K. A. Takeuchi and M. Sano, J. Stat. Phys. **147**, 853 (2012).
[4] K. A. Takeuchi, Physica A **504**, 77 (2018).
[5] Y. T. Fukai and K. A. Takeuchi, Phys. Rev. Lett. **119**, 030602 (2017).
[6] P. G. de Gennes and J. Prost, *The Physics of Liquid Crystals* (Oxford University Press, U.S.A., Oxford, 1995).
[7] D. T. Gillespie, Phys. Rev. E **54**, 2084 (1996).
[8] M. Prähofer and H. Spohn, J. Stat. Phys. **108**, 1071 (2002).
[9] J. Hägg, Ann. Probab. **36**, 1059 (2008).
[10] L. Beghin and E. Orsingher, Lith. Math. J. **39**, 157 (1999).
[11] I. M. Johnstone and Z. Ma, Ann. Appl. Probab. **22**, 1962 (2012).
[12] K. Johansson, Commun. Math. Phys. **242**, 277 (2003).
[13] I. Corwin, J. Quastel, and D. Remenik, Commun. Math. Phys. **317**, 347 (2013).